ACSNANO
www.acsnano.org
ARTICLE

Superconducting Ferromagnetic Nanodiamond

Gufei Zhang,[*,†,●] Tomas Samuely,[‡,●] Zheng Xu,[§,●] Johanna K. Jochum,[∥] Alexander Volodin,[∥] Shengqiang Zhou,[⊥] Paul W. May,[▽] Oleksandr Onufriienko,[‡] Jozef Kačmarčík,[‡] Julian A. Steele,[#] Jun Li,[○] Johan Vanacken,[†] Jiri Vacík,[∞] Pavol Szabó,[‡] Haifeng Yuan,[¶] Maarten B. J. Roeffaers,[#] Dorin Cerbu,[†] Peter Samuely,[‡] Johan Hofkens,[¶] and Victor V. Moshchalkov[*,†]

[†]INPAC-Insititute for Nanoscale Physics and Chemistry and [∥]Laboratory of Solid State Physics and Magnetism, KU Leuven, Celestijnenlaan 200D, B-3001 Heverlee, Belgium

[‡]Centre of Low Temperature Physics, Institute of Experimental Physics, Slovak Academy of Sciences and Faculty of Science, P. J. Safarik University, 04001 Kosice, Slovakia

[§]School of Electrical and Computer Engineering, University of California, Davis, California 95616, United States

[⊥]Institute of Ion Beam Physics and Materials Research, Helmholtz-Zentrum Dresden-Rossendorf, Bautzner Landstr. 400, 01328 Dresden, Germany

[▽]School of Chemistry, University of Bristol, Bristol BS8 1TS, United Kingdom

[#]Centre for Surface Chemistry and Catalysis and [¶]Department of Chemistry, KU Leuven, Celestijnenlaan 200F, B-3001 Heverlee, Belgium

[○]Research Institute of Superconductor Electronics, Nanjing University, 210093 Nanjing, China

[∞]Nuclear Physics Institute, Academy of Sciences of the Czech Republic, 25068 Husinec-Rez, Czech Republic

Supporting Information

ABSTRACT: **Superconductivity and ferromagnetism are two mutually antagonistic states in condensed matter. Research on the interplay between these two competing orderings sheds light not only on the cause of various quantum phenomena in strongly correlated systems but also on the general mechanism of superconductivity. Here we report on the observation of the electronic entanglement between superconducting and ferromagnetic states in hydrogenated boron-doped nanodiamond films, which have a superconducting transition temperature $T_c \sim 3$ K and a Curie temperature $T_{Curie} > 400$ K. In spite of the high T_{Curie}, our nanodiamond films demonstrate a decrease in the temperature dependence of magnetization below 100 K, in correspondence to an increase in the temperature dependence of resistivity. These anomalous magnetic and electrical transport properties reveal the presence of an intriguing precursor phase, in which spin fluctuations intervene as a result of the interplay between the two antagonistic states. Furthermore, the observations of high-temperature ferromagnetism, giant positive magnetoresistance, and anomalous Hall effect bring attention to the potential applications of our superconducting ferromagnetic nanodiamond films in magnetoelectronics, spintronics, and magnetic field sensing.**

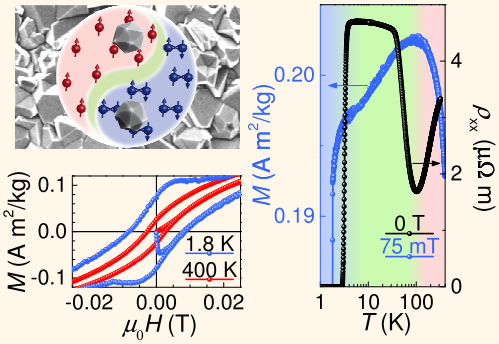

KEYWORDS: *nanodiamond, superconductivity and ferromagnetism, spin fluctuations, giant positive magnetoresistance, anomalous Hall effect*

Apart from being a symbol of wealth, prestige, and love, diamond is increasingly being recognized as a piece of jewelry for science and technology, due to a broad spectrum of its properties and wide ranging applications.[1] The extraordinarily high breakdown voltage and thermal conductivity, remarkable inertness to chemicals and contamination, and tunable electronic properties upon doping make diamond not only a drilling tool for mining and machinery but also a promising candidate for the next-generation high-speed high-power electronics.[1−3] Cost-effective diamond films, prepared by the wafer-scale growth of diamond using chemical vapor deposition (CVD), can be integrated into the mature

Received: March 9, 2017
Accepted: May 16, 2017
Published: May 16, 2017

DOI: 10.1021/acsnano.7b01688
ACS Nano 2017, 11, 5358−5366

silicon industry and shaped into various high-technology devices.[2−6]

The most effective method to tune the electronic properties of diamond is to introduce substitutional boron dopants into this material. Upon doping, diamond undergoes the insulator−metal transition when the boron concentration is about 3×10^{20} cm^{-3}.[7] At even higher boron doping levels, diamond becomes superconducting.[4,8] These phase transitions in diamond can be roughly traced by its color change, *i.e.*, light blue for semiconducting diamond, blue for diamond in the metallic regime, and black for superconducting diamond. The discovery of superconductivity in doped diamond has triggered a series of experimental and theoretical studies of the Cooper pairing mechanism in doped semiconductors, while no conclusion has been reached due to the limits of different experimental and theoretical methods. On one side, scanning tunneling microscopy/spectroscopy (STM/S) measurements on black diamond suggested phonon-mediated pairing in the weak coupling limit, based on the match between the theoretical and experimental values of the Bardeen−Cooper−Schrieffer (BCS) ratio. On the other hand, the fact that the emergence of superconductivity coincides with the doping-driven insulator−metal transition in diamond appears to validate the resonant valence band theory and indicate correlation-driven Cooper pairing in black diamond.[9] In the latter case, singlet coupling between spins of neighboring boron acceptors was considered as the seed of pairing.[10] Furthermore, despite the three-dimensional nature, significant variability in its physical properties has been observed in boron-doped diamond, *e.g.*, the broad range of the superconducting transition temperature T_c,[4,7−14] the pronounced difference in the normal state resistivity,[4,7−14] and anomalous resistance peaks and dips.[2,7,11] The cause of this variability lies in the specific synthesis method, growth mode, and post-treatment of the diamond.

Synthetic-doped diamond can be not only superconducting but also ferromagnetic. Theoretical modeling based on first principle calculations has demonstrated that the hydrogen incorporation can turn a metal-free diamond into a ferromagnet.[15] Meanwhile, ferromagnetism has also been reported *via* bulk magnetization measurements for diamond that has been bombarded with nitrogen or carbon ions. This effect has been attributed to the bonding defects and mixture of sp^2/sp^3 carbon created by the ion damage.[16,17] Hydrogenation and sp^2/sp^3 defects have been generally employed to explain the intrinsic ferromagnetism observed in other forms of carbon as well, *e.g.*, fullerenes,[18] graphene,[19] carbon nanotubes,[20] and graphite.[21] Taking graphene for instance, first principle calculations based on spin-polarized density functional theory have demonstrated that semihydrogenation of a graphene sheet will result in the localization of electrons at the unhydrogenated carbon sites, and the uncompensated spin polarizations at these sites will turn the system into a ferromagnet.[22]

Here we report on the investigation of the interplay between ferromagnetism and electrical transport in hydrogenated and heavily boron-doped nanodiamond (HBD) films, which have a Curie temperature of $T_{Curie} > 400$ K. In spite of the presence of the ferromagnetic ordering, the superconducting state still develops in our HBD films at $T_c \sim 3$ K. The magnetization and resistivity data of the HBD demonstrate at different temperatures important correlations, suggesting spin-dependent electrical transport and possible Cooper pairing due to spin fluctuations in the HBD films. Furthermore, the significant magnetic remanence well above room temperature, the anomalous Hall effect, and the giant positive low-field magnetoresistance, observed in our HBD films, bring attention to the potential applications of this material in different areas, *e.g.*, magnetoelectronics, spintronics, and magnetic field sensing.

RESULTS AND DISCUSSION

The HBD films were deposited on SiO_2/Si substrates (undoped Si with 300 nm-thick SiO_2 on top) in a hot filament CVD reactor (see Experimental Section). Grazing incidence X-ray diffraction (GIXRD) was used for phase identification of the HBD films. Besides the Si (311) peak of the substrate, only diffraction peaks from polycrystalline diamond are found in the GIXRD spectrum (see Figure 1A). In addition, our secondary ion mass spectrometry (SIMS) measurements on the HBD films did not detect metallic impurities or anything other than carbon−hydrogen species within the detection limit (see Supporting Information Figure S1). Neutron depth profiling (NDP) analysis indicates that the film thickness is ∼900 nm, and the boron concentration $n_{boron} \sim 1.5 \times 10^{21}$ cm^{-3}, well above the critical

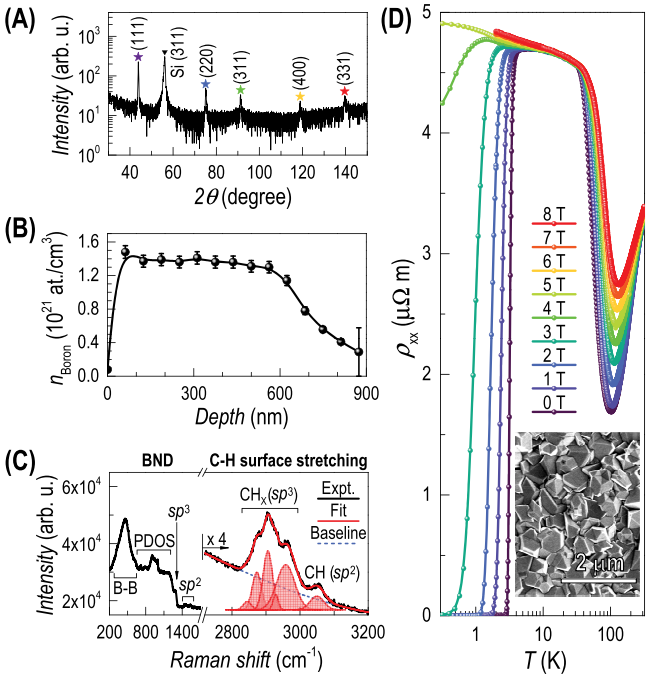

Figure 1. Structural analysis and the longitudinal thermoresistivity $\rho_{xx}(T)$ of the HBD films. (A) In the grazing incident X-ray diffraction spectrum, only diffraction peaks from diamond (colored stars) and the Si substrate (inverted triangle) are found, revealing the polycrystalline structure of the HBD and the absence of impurity phases. (B) Neutron depth profiling analysis indicates that the HBD film thickness is about 900 nm, and the boron concentration is around 1.5×10^{21} cm^{-3}. (C) Raman scattering spectrum, excited with a 488 nm laser, confirms the successful surface hydrogenation of the HBD. For clarity, the two regions of significance, *i.e.*, the boron-doped nanodiamond (BND) modes and the carbon−hydrogen (C−H) surface modes, are emphasized, with the latter being resolved and rescaled (×4). B−B: boron−boron dimer/cluster vibrations. PDOS: the disorder-activation of otherwise forbidden diamond phonon density of states. For CH_x, $x = 1-3$. (D) $\rho_{xx}(T)$ demonstrates a resistive superconducting transition at low temperature with the offset critical temperature $T_c^{offset} = 3$ K and an anomalous dip at around 100 K. Both the superconducting transition and the anomalous dip are suppressed by applied magnetic fields. Inset: scanning electron micrograph displaying the granular morphology of the HBD.

DOI: 10.1021/acsnano.7b01688
ACS Nano 2017, 11, 5358−5366

doping level for the insulator–metal transition in diamond (see Figure 1B).[7]

To analyze the hydrogenated surface, we investigated the HBD films by Raman scattering. Figure 1C presents a characteristic Raman spectrum recorded from the HBD surface. The spectrum is partitioned into two areas of significance: low-frequency diamond vibrational modes, and a high-frequency band associated with carbon–hydrogen stretching vibrations originating from the hydrogenated surface. Note that similar spectra were obtained from both the undersurface (*i.e.*, after the Si substrate had been chemically removed) and the upper surface of the HBD films. The two low-energy bands, centered at approximately 450 and 1200 cm^{-1}, are caused by localized boron–boron dimer/cluster vibrations and the disorder-activation of otherwise forbidden diamond phonon density of states (PDOS), respectively.[23,24] In addition to the diamond peak located at 1332 cm^{-1}, a weak G band appears near 1500 cm^{-1} due to the presence of sp^2 carbon bonding at the diamond grain boundaries.[25]

The high-energy modes between 2800 and 3100 cm^{-1} are the well-known signatures of a hydrogenated diamond surface and the stretching vibrations of carbon–hydrogen surface bonds.[26−28] The prominent features, which are resolved just above 2800 cm^{-1}, originate from a combination of symmetric and asymmetric carbon–hydrogen stretching with sp^3-hybridization.[27] A smaller peak at 3050 cm^{-1} also arises from carbon–hydrogen bonding, although from carbon in a sp^2-hybridization, and likely contributes to the bands at approximately 1500 cm^{-1}.[29] The relatively high strength of the carbon–hydrogen surface Raman modes, as well as its presence over the entire HBD surface, confirms the successful hydrogenation of the sample surface.

We performed four-probe ac measurements on the HBD films to characterize their electrical transport properties. Figure 1D shows the characteristic longitudinal thermoresistivity $\rho_{xx}(T)$ of the HBD films in different applied magnetic fields $\mu_0 H$. In zero magnetic field, when lowering T from 320 K, the resistivity decreases and reaches a minimum at about 100 K. Further decrease of T brings about a steep increase of $\rho_{xx}(T)$ within the temperature window of 30–100 K. As a result, the $\rho_{xx}(T)$ curve demonstrates a sharp dip at about 100 K. Below 30 K, a slight increase in $\rho_{xx}(T)$ is followed by the resistive superconducting transition with T_c^{offset} = 3 K (T_c^{offset} is the offset critical temperature at which ρ drops to 0). Note that similar $\rho_{xx}(T)$ dips with much smaller amplitude have been previously reported for boron-doped diamond films grown by microwave plasma-enhanced CVD.[7] Both the superconducting state at low temperature and the anomalous $\rho_{xx}(T)$ dip at high temperature are suppressed by the applied magnetic field (see Figure 1D).

Based on the magnetic field dependence of $\rho_{xx}(T)$, we constructed the $\mu_0 H_{c2}$–T phase diagram for the superconducting state (see Figure 2). A quadratic fit to the $\mu_0 H_{c2}$–T phase boundary yields $\mu_0 H_{c2}(0\ K)$ = 4.3 T and thus the Ginzburg–Landau coherence length $\xi_{GL} = [\Phi_0/2\pi H_{c2}(0\ K)]^{1/2}$ = 8.7 nm with $\Phi_0 = h/2e$ being the flux quantum. The same $\mu_0 H_{c2}(0\ K)$ and ξ_{GL} values are obtained from the linear fit to the phase boundary, following the standard relationship for a dirty type-II superconductor $H_{c2}(0\ K) = -0.69 T_c (dH/dT)|_{T_c}$.

Consistent with the $\rho_{xx}(T)$ data, giant positive magnetoresistance (PMR) was observed when measuring the longitudinal resistivity as a function of magnetic field $\rho_{xx}(H)$ at temperatures around the $\rho_{xx}(T)$ dip (see Figure 3A). The largest

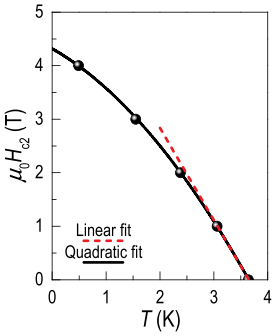

Figure 2. Bulk upper critical field $\mu_0 H_{c2}$ of the HBD. The criterion is set at 95%$\rho_{10\ K}$ in the $\rho_{xx}(T)$ plots to extract the temperature dependence of $\mu_0 H_{c2}$. Quadratic and linear fits to the $\mu_0 H_{c2}$–T phase boundary yield the same $\mu_0 H_{c2}(0\ K)$ value of 4.3 T.

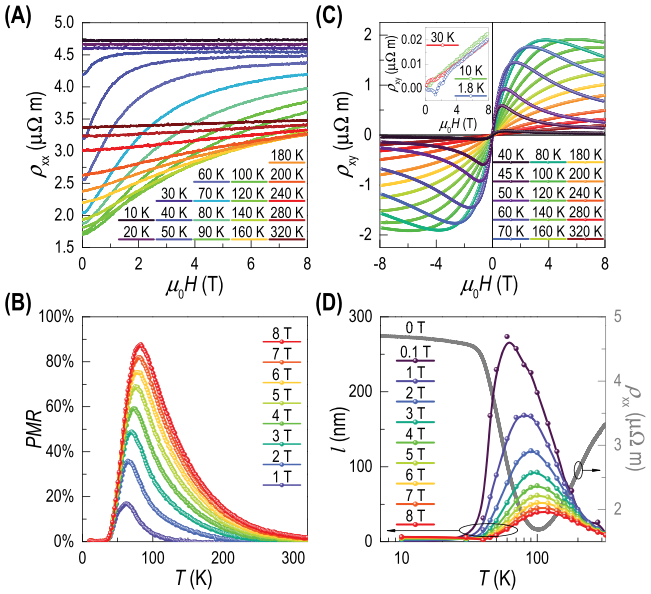

Figure 3. Longitudinal magnetoresistivity $\rho_{xx}(H)$, the PMR, the transverse resistivity $\rho_{xy}(H)$, and the mean free path l of the HBD films. (A) Magnetic field dependence of the longitudinal resistivity. (B) Giant PMR is observed in the temperature window, where the anomalous $\rho_{xx}(T)$ dip is located. (C) In the same temperature window, $\rho_{xy}(H)$ demonstrates anomalous Hall effect. (D) The mean free path, deduced from the $\rho_{xx}(H)$ and $\rho_{xy}(H)$ measurements, is plotted together with the anomalous $\rho_{xx}(T)$ dip. The anomalous $\rho_{xx}(T)$ behavior is translated into strong variation of the mean free path.

PMR = $[\rho_{xx}(H) - \rho_{xx}|_{H=0}]/\rho_{xx}|_{H=0}$ goes up to nearly 90% at about 83 K when $\mu_0 H$ = 8 T (see Figure 3B). The strong temperature dependence of the electrical transport properties is also revealed in the Hall effect measurements. Figure 3C shows the transverse resistivity $\rho_{xy}(H)$ measured at different temperatures. Below 30 K, linear $\rho_{xy}(H)$ behavior is found at the normal state, while anomalous Hall effect (AHE) appears at high temperatures where the $\rho_{xx}(T)$ dip is located.

AHE has been generally observed in ferromagnetic semiconductors and oxides,[30] and its origin still remains an open question. The nonlinear $\rho_{xy}(H)$ behavior has been either attributed to the magnetic field-dependent ratio between the mobility of holes and electrons based on the compensation effects[31] or interpreted as a result of superposition of the ordinary Hall effect and the magnetic scattering mechanism.[32] Note that the two

DOI: 10.1021/acsnano.7b01688
ACS Nano 2017, 11, 5358–5366

techniques involved in our preparation of the HBD films, *i.e.*, boron doping and hydrogenation, are both well-known approaches to achieve *p*-type conduction in diamond.[33] Furthermore, although the intergrain sp^2 medium (about 1% in our HBD) can be a source of electrons, no AHE so far has been reported for other granular diamond systems which are also rich in intergrain sp^2 phases.[34,35] The AHE observed in our HBD films is, therefore, most likely due to the magnetic scattering in the samples.

The anomalous $\rho_{xx}(T)$ data can be translated into strong variation of the mean free path. Based on the $\rho_{xx}(H)$ and $\rho_{xy}(H)$ data, we deduced the mean free path $l = \hbar k_F \tau/m^*$ of the free carriers by assuming contributions from *p*-type carriers only. Here $\hbar$ is the Planck constant, $k_F = (3\pi^2 n)^{1/3}$ is the Fermi wave vector under a spherical Fermi surface approximation with n being the carrier density, τ the mean free time, and m^* the effective mass of the carriers. To eliminate τ/m^*, the Boltzmann conductivity $\sigma = nq^2\tau/m^*$ is introduced into the expression for l:

$$l = \hbar(3\pi^2)^{1/3}\frac{\sigma}{n^{2/3}q^2} = \frac{\hbar(3\pi^2)^{1/3}R_H{}^{2/3}}{q^{4/3}\rho_{xx}} \quad (1)$$

where q is the elementary charge, and R_H is the Hall coefficient.[36] This calculated value of l is plotted as a function of T and $\mu_0 H$ in Figure 3D, to which the $\rho_{xx}(T)|_{H=0}$ curve is added for reference.

When looking into the underlying physics of the anomalous $\rho_{xx}(T)$ dip *via* bulk magnetization measurements, ferromagnetism was found in our HBD films. Figure 4A shows the magnetization hysteresis loops $M(H)$ before subtraction of the linear diamagnetic background of the substrate. After eliminating the substrate signal and normalizing the HBD signal to the HBD mass, the low-field $M(H)$ of significance is plotted in Figure 4B,C to provide a clear view of the temperature-induced evolution of the central peak, the virgin curve, and the coercivity. The $M(H)$ loops, measured at $T < T_c^{offset}$, demonstrate a central peak superimposed on a ferromagnetic background around zero field. The central peak diminishes as the temperature is increased, leaving the ferromagnetic signal behind at higher temperatures (see Figure 4B,C). A similar scenario takes place in the virgin curve as well. The V-shaped virgin curve diminishes and ends up with a conventional ferromagnetic feature above T_c^{offset}. Analysis of the virgin curves yields a lower critical field of $\mu_0 H_{c1} \sim 0.5$ mT at $T = 0$ (see Figure 5).

As shown in the inset to Figure 6A, a sudden increase begins in the coercive field $\mu_0 H_{CF}$ when the temperature is lowered to T_c^{offset}. In contrast to the data for a nonmagnetic superconductor,[14] the zero-field cooling (ZFC) and field cooling (FC) curves of our HBD, measured at 5 mT, remain separated from each other throughout the entire temperature range of 1.8−400 K (see Figure 6A), suggesting the presence of ferromagnetism with $T_{Curie} > 400$ K in addition to the superconducting transition around $T_c^{offset} = 3$ K. We measured the ZFC and FC magnetization as a function of temperature in different applied magnetic fields (see Figure 6B). When increasing the magnetic field, the superconducting state is gradually suppressed, and the ZFC and FC curves start merging at high temperatures. Our bulk magnetization data clearly reveal the coexistence of superconductivity and ferromagnetism in the HBD films.

To gain further insight into the ferromagnetism and its interplay with the superconductivity in the HBD films, we performed direct local measurements with magnetic force microscopy (MFM) and STM/S, respectively. Granular diamond films

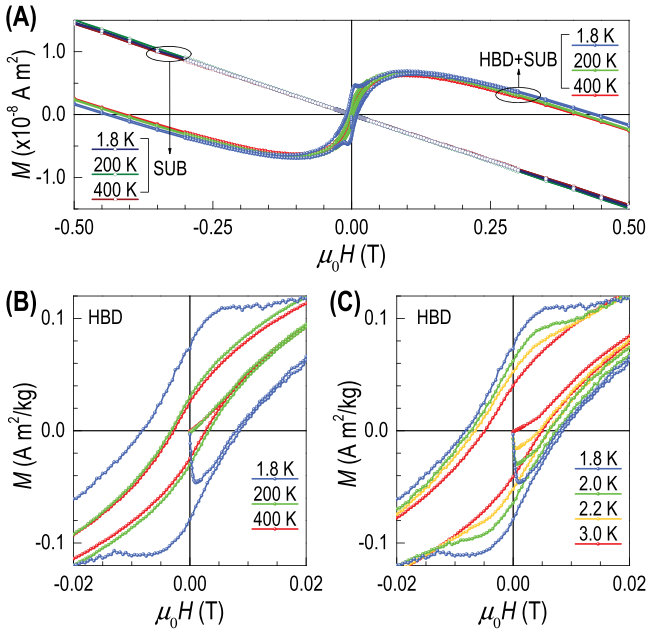

Figure 4. Magnetization *versus* applied magnetic field, indicating the coexistent ferromagnetism and superconductivity in the HBD. (A) Magnetization hysteresis loops $M(H)$ measured at different temperatures for the substrate (SUB) and the HBD grown on the substrate (HBD + SUB). As evidenced by its linear $M(H)$, the substrate is simply diamagnetic throughout the entire temperature range. (B) After eliminating the diamagnetic background signal of the SUB, the $M(H)$ is normalized to the mass of the HBD. The $M(H)$, measured below 3 K, demonstrates a central peak and a V-shaped virgin curve which are superimposed on a ferromagnetic background. Ferromagnetic $M(H)$ is seen up to 400 K. (C) The central peak and the V-shaped virgin curve smear out at higher temperatures, leaving behind the ferromagnetic signal above 3 K.

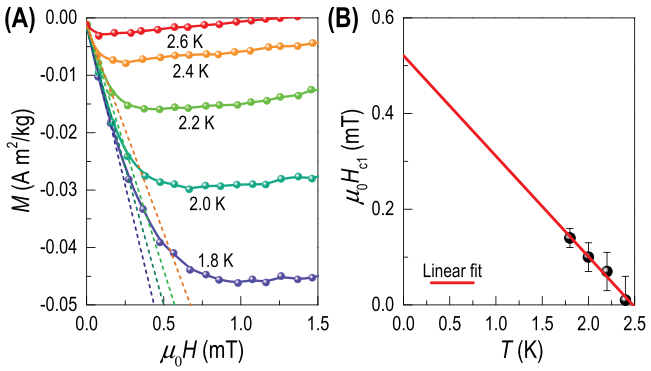

Figure 5. Bulk lower critical field $\mu_0 H_{c1}$ of the HBD. (A) Virgin curves of the $M(H)$ measured at different temperatures. By recording the magnetic fields, at which the virgin curves deviate from the linear behavior (the dashed lines), we build up the $\mu_0 H_{c1}$−T phase boundary in (B). Linear fit to the $\mu_0 H_{c1}$−T phase boundary yields $\mu_0 H_{c1}(0\ K) = 0.52$ mT.

such as our HBD generally have an upper surface roughness comparable to the film thickness due to the growth mode of this material. To minimize the influence of the surface roughness on the local measurements, the MFM and STM/S measurements were carried out on the relatively flat undersurface.

Direct evidence for the presence of ferromagnetism in our HBD was provided by the MFM measurements at room temperature. Figure 7A−C displays the topography of a 10 μm × 10 μm

DOI: 10.1021/acsnano.7b01688
ACS Nano 2017, 11, 5358−5366

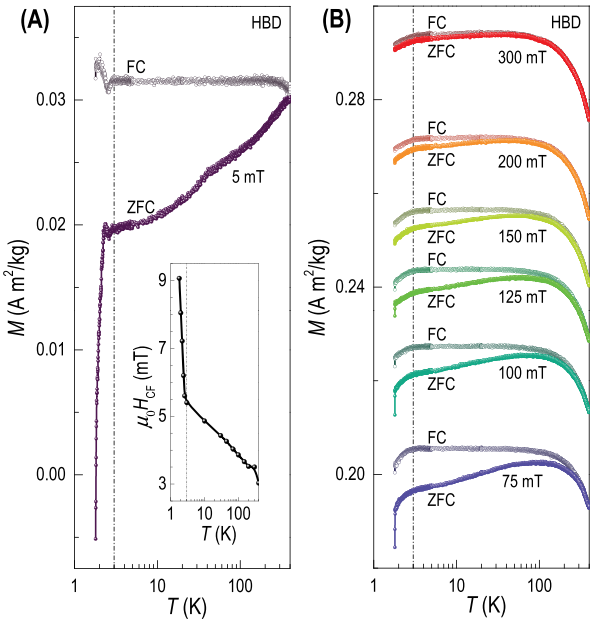

Figure 6. Magnetization *versus* temperature, indicating that in spite of the presence of the ferromagnetic ordering, the superconducting state still develops in our HBD films at $T_c \sim 3$ K. (A) Magnetization *versus* temperature $M(T)$ measured in ZFC and FC processes. The ZFC and FC curves show a superconducting transition at about 3 K (the dash-dotted line) and remain separated from each other up to 400 K. Inset: Coercive field *versus* temperature $\mu_0 H_{CF}(T)$. (B) $M(T)$ measured in different applied magnetic fields. When increasing the magnetic field, the ZFC and FC curves start merging at high temperatures.

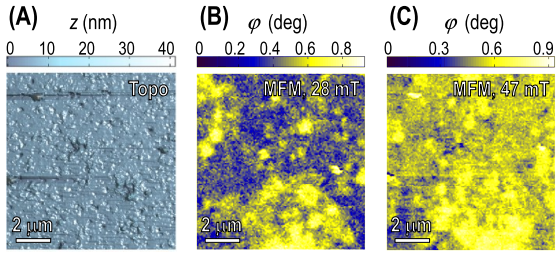

Figure 7. MFM images taken at room temperature for the undersurface of the HBD. (A) Topography of a 10 μm × 10 μm area of the HBD undersurface, obtained by atomic force microscopy. (B and C) MFM images of the same area, taken at 28 mT and 47 mT, respectively. The frequency shift φ (in degrees) represents the strength of the near-surface stray field produced by the HBD.

undersurface and the corresponding MFM images of this area, respectively. Since MFM measures the vertical component of the force gradient between the sample and the tip, it is sensitive to the strength and polarity of near-surface stray fields produced by ferromagnetic samples. As shown in Figure 7A–C, our MFM data demonstrate clear magnetic contrasts in different magnetic fields and show no correlation between the topography and the magnetic structures, revealing the intrinsic ferromagnetism of the HBD.

The origin of the ferromagnetism in metal-free carbon allotropes still remains a subject of debate. It was first argued that bonding defects in sp^2 and sp^3 mixtures are responsible for the ferromagnetism observed in bombarded graphite and diamond.[16,17] Later, the ferromagnetism in carbon-based materials was found to be intrinsic and linked to hydrogen at the surface, based on detailed studies using X-ray magnetic circular dichroism.[21] In our HBD films, both bonding defects and hydrogen are present. The grain boundaries of polycrystalline diamond are known to be rich in sp^2 and sp^3 mixtures.[14] Taking into account the absence of ferromagnetism in polycrystalline bulk diamond prepared using the high-temperature high-pressure method (a synthetic process in which no hydrogen is involved),[14] hydrogen incorporation at the surfaces and interfaces is more likely to be the cause of the ferromagnetism observed in our HBD films.

To gain further insight into the competing interplay between the superconductivity and ferromagnetism in the HBD films, we simultaneously acquired the conductance map and the topography of the HBD undersurface with STM/S in the current-imaging tunneling spectroscopy (CITS) mode and in constant-current mode, respectively.[37] By normalizing the differential conductance spectra $G(V_b) = dI/dV$ to a value far outside the superconducting gap and collecting the $G_{zb} = G(V_b = 0)$ values, we built up so-called zero-bias conductance G_{zb} maps in combination with the corresponding topography (see Figure 8A, for example).

Figure 8A–D shows the magnetic field-induced evolution of the G_{zb} map from a characteristic area at 0.5 K. When $\mu_0 H = 0$ T, the G_{zb} is rather homogeneous and equal to zero, indicating a full superconducting gap across the whole area (see Figure 8A). Upon applying a magnetic field, the G_{zb} map separates into two main regions: a bluish one with lower G_{zb} and a reddish one with higher G_{zb} (see Figure 8C). The spatial variations of G_{zb} (the modulations of the superconducting order parameter Δ) have also previously been observed in nonferromagnetic diamond and were explained as resulting from the granular disorder and/or intragrain "uniform" disorder.[14] In our superconducting ferromagnetic HBD, variations of the local magnetic structure (see Figure 7B,C) can also be a cause of this phenomenon. By further increasing $\mu_0 H$, the superconductivity in the whole scanned area was gradually suppressed, resulting in $G_{zb} = 1$ at nearly every spot (see Figure 8D).

Figure 8E shows the normalized differential conductance spectra $G_{norm}(V_b)$ recorded from a characteristic spot ⊕ (see Figure 8A–D). The gradual destruction of superconductivity in higher magnetic fields is responsible for the in-gap states and the suppression of the coherence peaks. The magnetic field-induced evolution of G_{zb} is summarized in Figure 8F. In all cases, G_{zb} remains zero below ~0.05 T (see Figure 8B,F) and then increases linearly to almost unity at higher magnetic fields, *i.e.*, at ~0.2 T for the ⊗ region and at ~0.3 T for the ⊕ region. Note that the effective shielding of the applied magnetic field at $\mu_0 H \leq 0.05$ T cannot be due to Meissner expulsion, since this field is larger than $\mu_0 H_{c1} \sim 0.5$ mT by two orders of magnitude. In contrast, magnetic field compensation can give rise to the shielding effect, *i.e.*, the applied magnetic field is compensated by the stray field of the ferromagnetic HBD.

We performed STS measurements over several areas across the whole sample surface and found no superconductivity above 0.4 T, which clearly demonstrates that the surface critical field of our HBD is one order of magnitude smaller than the bulk critical field of ~4 T, as obtained from the $\rho_{xx}(T)$ measurements (see Figure 1D). We also emphasize that for a nonferromagnetic diamond with similar T_c^{offset} and normal-state resistivity ρ_{norm} ($T_c^{offset} \sim 3$ K; $\rho_{norm} \sim 18\ \mu\Omega$ m), the surface critical field is of the same order of magnitude as the bulk value ~4–5 T.[14]

As already discussed above, the critical magnetic field of the HBD surface is unusually small in comparison with the bulk

DOI: 10.1021/acsnano.7b01688
ACS Nano 2017, 11, 5358–5366

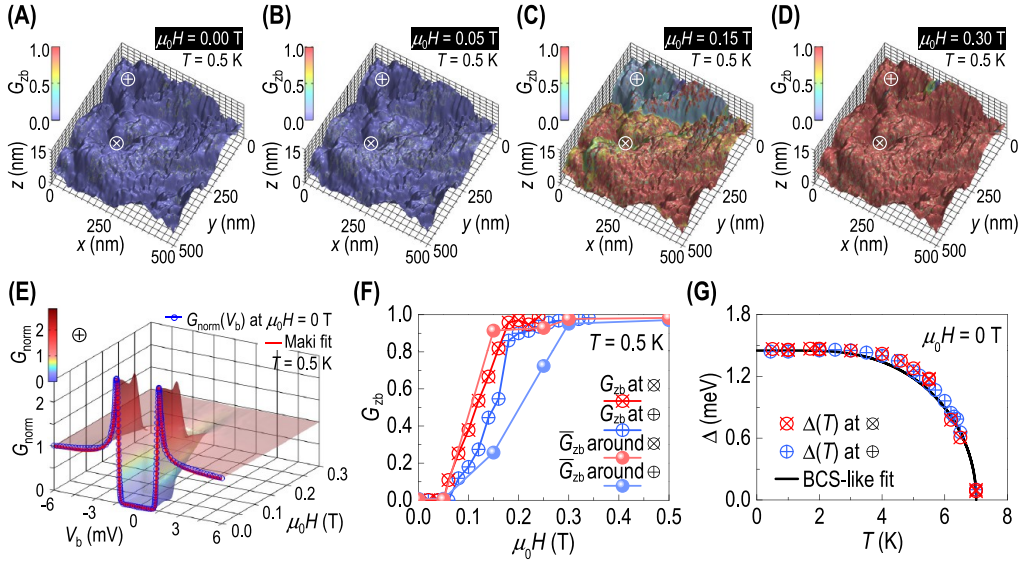

Figure 8. Magnetic field- and temperature-induced evolution of the superconducting gap in STM/S measurements. (A–D) Combined topography and zero-bias conductance G_{zb} maps of the HBD undersurface at 0.5 K in different applied magnetic fields. The small patch, remaining blue/green in (D), is the undoped insulating diamond seed which acted as a tunneling barrier (see Supporting Information Figure S2) and served as a position marker for our STM/S measurements. (E) Magnetic field-induced evolution of the characteristic differential conductance spectra taken at location ⊕ in (A–D). The $G_{norm}(V_b)$ curve, measured at $\mu_0H = 0$ T, is fitted to the density of states, as obtained from the Maki formalism convoluted with the Fermi distribution function. (F) Magnetic field-induced evolution of G_{zb} at different locations. The mean zero-bias conductance values $\bar{G}_{zb}$ are calculated by averaging the G_{zb} of 1000 spots around ⊗ and ⊕, respectively. (G) Temperature-induced evolution of the superconducting gap at locations ⊕ and ⊗. The STM/S data indicate an unusually small surface critical field of ~0.3 T in our HBD.

critical magnetic field. The same conclusion can be drawn when taking into account the superconducting gap size 2Δ and the local critical temperature T_c(local). We measured the temperature-induced evolution of $G(V_b)$ at $\mu_0H = 0$ T, from which the $\Delta(T)$ values are deduced. The $\Delta(T)$ of spots ⊗ and ⊕ are then fitted by a BCS-like $\Delta(T)$ dependence in Figure 8G. Despite the difference between their critical field (see Figure 8A–D), both spots have the same $\Delta(0\text{ K}) = 1.45$ meV and T_c(local) = 7 K within the limits of experimental error. Similar Δ and T_c(local) values were observed across the whole sample. Accordingly, in the absence of ferromagnetism, an applied magnetic field higher than 10 T will be needed to fully suppress the superconductivity at the HBD surface.[11] This is obviously not the case, as evidenced by our STM/S measurements in different applied magnetic fields (see Figure 8A–F). Notably, the ratio $2\Delta(0\text{ K})/k_BT_c$(local) = 4.8 is 36% larger than the conventional BCS theory value, indicating that our HBD films are situated in the strong coupling regime.

Figure 9 shows the fits of different models to $G(V_b)$ measured at $\mu_0H = 0$ T. Using the Maki formalism convoluted with the Fermi distribution function,[38] we are able to reproduce the reduced singularities in the measured coherence peaks, while retaining the full superconducting gap, suggesting pair breaking potentially caused by magnetic effects. Such consistency is unattainable by using the thermally smeared density of states given by the BCS theory or its Dynes modification.[39,40]

The two antagonistic strongly correlated states, superconductivity and ferromagnetism, are not electronically independent from each other but intimately entangled in our HBD. When plotting the electrical transport and magnetization data together (see Figure 10A), a correlation between the $\rho_{xx}(T)$ and $M(T)$ behaviors is found in different temperature windows. Above 100 K, our HBD demonstrates an overall ferromagnetic state with parallel-aligned spins in magnetic domains (see Figure 10B), and the transport of carriers with well aligned spins results in the

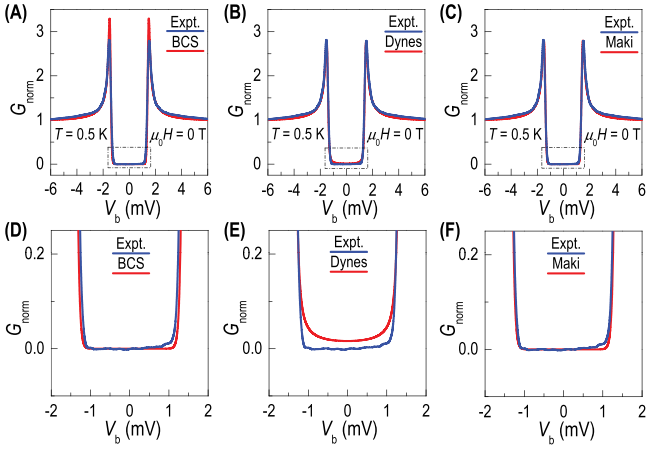

Figure 9. Fits of different models to $G_{norm}(V_b)|_{H=0\text{ T}}$ measured at spot ⊕. The experimental data (blue) are plotted together with the differential conductance calculated using three different models (red): (A) BCS model, where the single-particle density of states is smeared only by temperature-dependent Fermi–Dirac function; (B) Dynes modification of the BCS model, which employs the smearing parameter $\gamma = 0.024$ meV; and (C) Maki formalism employing the pair breaking parameter $\alpha = 0.011$ meV. The fitting results in the dashed boxes of (A–C) are magnified in (D–F), respectively.

metallic state (see the red-shadowed regime in Figure 10A). At low temperatures, besides boron-doping-induced superconductivity in diamond, Cooper pairing of the carriers with antiparallel-aligned spins at domain walls can also contribute to the formation of the superconducting state (see Figure 10D and the blue-shadowed regime in Figure 10A) in the framework of the so-called domain wall superconductivity,[41,42] a concept developed in line with the Anderson–Suhl theory.[43] In the Anderson–Suhl theory, a spin-singlet superconducting state can survive and

DOI: 10.1021/acsnano.7b01688
ACS Nano 2017, 11, 5358–5366

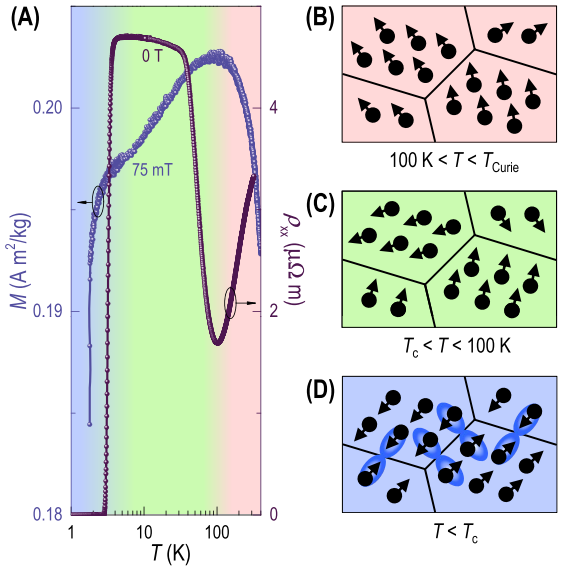

Figure 10. Correlation between $\rho_{xx}(T)$ and $M(T)$, indicating the electronic entanglement of the ferromagnetic and superconducting states and the presence of a precursor phase, in which spin fluctuations intervene for the development of the domain wall superconductivity at low temperatures. (A) The $\rho_{xx}(T)$ and $M(T)$ curves are roughly divided into three regions (shadowed in red, green and blue, respectively) with respect to the temperature coefficient of ρ_{xx} and M. The corresponding spin configurations are schematically illustrated in (B–D). (B) In the temperature window of 100 K < T < T_{Curie}, the overall ferromagnetism of the system results from the ferromagnetic arrangement of the domains (domain walls represented by the black lines). (C) The precursor phase emerges in the temperature window of T_c < T < 100 K, where spin fluctuations intervene in the system *via* antiferromagnetic arrangement of the domains. (D) When T < T_c, carriers with antiparallel-aligned spins can be an additional source for Cooper pairing (opposite arrows bound by blue ∞) at the domain walls, in addition to the boron-doping-induced superconductivity in the HBD.

coexist with an overall ferromagnetic state, as long as the coherence length is much larger than the size of the antiferromagnetically arranged domains. Under this precondition, charge carriers with opposite spin polarizations in different domains can form Cooper pairs at the domain walls. This theory may not be applied to our system in a direct sense, while in the physics picture of domain wall superconductivity,[41,42] narrow superconducting areas can emerge at the domain walls owing to the compensation of the stray fields of neighboring domains with antiparallel-aligned spins.[44−46] Accordingly, we schematically interpret the possible domain wall superconductivity in our system as shown in Figure 10D.

For our superconducting ferromagnetic HBD, in the case that the same charge carriers are involved in the development of the two phases as illustrated in Figure 10B,D (or in other words, the superconducting state is electronically entangled with the ferromagnetic state), a precursor phase will be required for the antiferromagnetic arrangement of the magnetic domains at low temperatures. The green-shadowed regime in Figure 10A shows exactly the precursor phase, in which spin fluctuations take place (see Figure 10C), as fingerprinted by the decrease in $M(T)$ when lowering the temperature. Note that in the absence of such an electronic entanglement and the domain wall superconductivity, the $M(T)$ should demonstrate a monotonic increase when lowering the temperature from T_{Curie}, which is, however, clearly not the case for our HBD. Here we emphasize the important role of spin fluctuations in developing the superconducting state and determining the electrical transport at low temperatures. The negative temperature coefficient of $\rho_{xx}(T)$, however, cannot be attributed to the spin fluctuations alone, since after all our HBD is a granular disordered system and the granular disorder-correlated localization effect should be also taken into account.[35]

CONCLUSION

In conclusion, the significant magnetic remanence well above room temperature, the giant positive low-field magnetoresistance (~90% above liquid-nitrogen temperature), and the pronounced anomalous Hall effect make our HBD a promising candidate for applications in not only power electronics and microelectronics but also magnetoelectronics, spintronics, and magnetic field sensing. Most importantly, the ferromagnetic ordering with T_{Curie} > 400 K and the superconducting ordering with T_c ~ 3 K, proven to be electronically entangled with each other, make our HBD also an interesting platform for investigating the competing interplay between the two antagonistic strongly correlated states of condensed matter. Our data indicate the presence of a precursor phase, in which spin fluctuations intervene and contribute to the superconducting transition at lower temperatures. The significant difference between the starting temperature of this precursor phase (~100 K) and T_c, however, raises an important question, *i.e.*, how does a ferromagnetic superconductor such as our HBD "foresee" its low-temperature superconducting "fate" and start "preparing" for the superconducting transition *via* antiferromagnetic arrangements of the magnetic domains at a much higher temperature? More thorough local measurements, *i.e.*, mapping of the spin polarizations and the density of states in the precursor phase, and theoretical modeling are needed to solve this mysterious problem.

EXPERIMENTAL SECTION

Synthesis of the HBD Films with Hot Filament CVD. The HBD films were synthesized in a hot filament CVD reactor. SiO_2/Si substrates (undoped Si with 300 nm-thick SiO_2 on top) were seeded with diamond powders (Ø ~ 15−25 nm), to generate nucleation sites for the diamond growth at 800 °C. A gas mixture, 0.6% CH_4 in H_2, was thermally dissociated at 2200 °C as the source of reactive hydrocarbon species. Boron doping was obtained by adding diborane (B_2H_6) to the gas mixture with a B_2H_6/CH_4 ratio of 5%. After 1 h deposition, the resulting boron-doped nanodiamond films had a thickness of ~900 nm and a mean grain size of ~800 nm (see inset, Figure 1D). The interface between diamond crystallites is believed to be only a few atoms thick and composed of a mixture of hydrogenated and unhydrogenated sp^2 and sp^3 carbon. Following deposition, the CH_4 and B_2H_6 gases were switched off while the sample remained under the filaments for 1 min in pure hydrogen gas, before being cooled to room temperature under H_2. This ensured that the surface was hydrogen terminated.[1] The as-deposited diamond films were directly used for our structural analysis (GIXRD, NDP, and Raman scattering), electrical transport, and bulk magnetization measurements. To perform Raman scattering, MFM, and STM/S measurements on the relatively flat undersurface of the HBD, the samples were marinated in 40% HF analar for 3 h to etch out the SiO_2 in between the HBD and Si. The freestanding HBD films, removed from the substrate, were then flipped over and placed onto nonmagnetic substrate for relevant experiments.

Phase Identification of the HBD Films by GIXRD. The GIXRD spectrum was collected by using a Panalytical X'pert Pro diffractometer with an incident angle of 2° for the incoming X-ray.

Determination of the Boron-Doping Level by NDP. Based on the thermal neutron-induced $^{10}B(n,\alpha)^7Li$ reaction, NDP was used to measure the depth dependence of the boron concentration.[35]

DOI: 10.1021/acsnano.7b01688
ACS Nano 2017, 11, 5358−5366

Confirmation of the HBD Surface Hydrogenation by Raman Scattering. Unpolarized micro-Raman scattering data were acquired in a quasi-backscattering configuration from the sample surface, employing a 20 mW argon ion gas laser operating at 488 nm, with the beam focused using a Zeiss 100×/1.3 oil objective. Raman spectra were dispersed *via* a triple grating system (300:300:500g/mm) in a subtractive configuration, and the Raman signals were recorded using a liquid-nitrogen-cooled CCD detector. The correct instrument calibration was verified by checking the position of the Si band at ±520.7 cm^{-1}.

Electrical Transport Measurements. The electrical transport properties of the HBD films were characterized in a Heliox ^{3}He cryostat (Oxford Instruments) and a physical property measurement system (Quantum Design). The same results were obtained from the four-probe ac and dc measurements on the HBD. No difference was seen between the data measured in a parallel magnetic field and in a perpendicular field, indicating that our HBD films are in the three-dimensional regime.

Bulk Magnetization Measurements. Magnetometry of the HBD was performed by using a MPMS3 (Quantum Design) system in Dresden for preliminary checks and another MPMS3 (Quantum Design) system in Leuven for detailed characterization. No difference was seen between the data measured in a parallel magnetic field and in a perpendicular field.

Magnetic Force Microscopy (MFM). MFM measurements were performed with a Dimension 3100D scanning probe microscope (Bruker) operated in the tapping lift mode. Commercial MFM probes PPP-MFMR (Nanosensors) with a remanence tip magnetization of ~3×10^5 A m^{-1} aligned along the tip axis were used. During the scanning procedure, the MFM probe-cantilever resonant frequency (~60 kHz) shifts were proportional to vertical gradients of the magnetic forces acting on the tip. These frequency shifts φ (in degrees) were detected as the cantilever's phase of oscillation relative to its actuator drive. In the tapping lift mode, the first scan was performed to obtain the topography by scanning the tip near the sample surface. During the second scan, MFM lifted the tip and maintained a constant tip−sample distance of ~50 nm. Thus, from the second scan, a topography-free MFM signal was acquired.

Scanning Tunneling Microscopy/Spectroscopy (STM/S). STM/S experiments were carried out by means of a sub-Kelvin STM system. Atomically sharp STM tips were formed *in situ* by controlled contact of the Au tip with a clean Au surface at cryogenic temperatures.[47] Since the Au tip has a constant density of states, the acquired $G(V_b)$ spectra represent the local density of states of the sample, and the G_{zb} maps reflect the spatial variation of the superconducting gap. Surface topography was acquired in the constant current mode with tunneling resistance of 500 kΩ. Magnetic fields were applied perpendicular to the HBD surface for the field-induced evolution of $G(V_b)$.

ASSOCIATED CONTENT

Supporting Information

The Supporting Information is available free of charge on the ACS Publications website at DOI: 10.1021/acsnano.7b01688.

Additional information on the SIMS and STM/S data (PDF)

AUTHOR INFORMATION

Corresponding Authors

*E-mail: Gufei.Zhang@kuleuven.be.

*E-mail: Victor.Moshchalkov@kuleuven.be.

ORCID

Gufei Zhang: 0000-0002-0150-5452

Paul W. May: 0000-0002-5190-7847

Haifeng Yuan: 0000-0001-6652-3670

Johan Hofkens: 0000-0002-9101-0567

Author Contributions

●These authors contributed equally.

Notes

The authors declare no competing financial interest.

ACKNOWLEDGMENTS

G.Z., J.Van., D.C., and V.V.M. acknowledge support from the Methusalem Funding by the Flemish Government. G.Z. and H.Y. are postdoctoral research fellows of the FWO (Research Foundation-Flanders). G.Z., J.K.J., and J.Van. thank the Hercules Foundation. J.K.J is supported by the KU Leuven Research Fund (GOA/14/007 and IDO/11/007). T.S., O.O., J.K., P.Sz., and P.S. are supported by the Slovak National Grants (APVV-14-0605, VEGA 1/0409/15, VEGA 2/0149/16 and U.S. Steel Kosice) and the EU ERDF-ITMS 26220120047. S.Z. acknowledges support from the Helmholtz Association (grant no. VH-NG-713). P.W.M. thanks the UK EPSRC for funding. J.Vac. thanks the Grant Agency of CR [P108-12G-108] for support. M.B.J.R. acknowledges financial support from the FWO (grant G.0962.13 and G.0B39.15), KU Leuven Research Fund (C14/15/053) and the European Research Council for ERC-Stg LIGHT [307523].

REFERENCES

(1) May, P. W. Diamond Thin Films: A 21-st Century Material. *Philos. Trans. R. Soc., A* **2000**, *358*, 473−495.

(2) Zhang, G.; Samuely, T.; Kačmarčík, J.; Ekimov, E. A.; Li, J.; Vanacken, J.; Szabó, P.; Huang, J.; Pereira, P. J.; Cerbu, D.; Moshchalkov, V. V. Bosonic Anomalies in Boron-Doped Polycrystalline Diamond. *Phys. Rev. Appl.* **2016**, *6*, 064011.

(3) Gajewski, W.; Achatz, P.; Williams, O. A.; Heanen, K.; Bustarret, E.; Stutzmann, M.; Garrido, J. A. Electronic and Optical Properties of Boron-Doped Nanocrystalline Diamond Films. *Phys. Rev. B: Condens. Matter Mater. Phys.* **2009**, *79*, 045206.

(4) Takano, Y.; Nagao, M.; Sakaguchi, I.; Tachiki, M.; Hatano, T.; Kobayashi, K.; Umezawa, H.; Kawarada, H. Superconductivity in Diamond Thin Films well above Liquid Helium Temperature. *Appl. Phys. Lett.* **2004**, *85*, 2851−2853.

(5) Mandal, S.; Bautze, T.; Williams, O. A.; Naud, C.; Bustarret, E.; Omnès, F.; Rodière, P.; Meunier, T.; Bäuerle, C.; Saminadayar, L. The Diamond Superconducting Quantum Interference Device. *ACS Nano* **2011**, *5*, 7144−7148.

(6) Hantschel, T.; Demeulemeester, C.; Eyben, P.; Schulz, V.; Richard, O.; Bender, H.; Vandervorst, W. Conductive Diamond Tips with Sub-Nanometer Electrical Resolution for Characterization of Nano-electronics Device Structures. *Phys. Status Solidi A* **2009**, *206*, 2077−2081.

(7) Klein, T.; Achatz, P.; Kacmarcik, J.; Marcenat, C.; Gustafsson, F.; Marcus, J.; Bustarret, E.; Pernot, J.; Omnes, F.; Sernelius, Bo E.; Persson, C.; Ferreira da Silva, A.; Cytermann, C. Metal-Insulator Transition and Superconductivity in Boron-Doped Diamond. *Phys. Rev. B: Condens. Matter Mater. Phys.* **2007**, *75*, 165313.

(8) Ekimov, E. A.; Sidorov, V. A.; Bauer, E. D.; Mel'nik, N. N.; Curro, N. J.; Thompson, J. D.; Stishov, S. M. Superconductivity in Diamond. *Nature* **2004**, *428*, 542−545.

(9) Blase, X.; Bustarret, E.; Chapelier, C.; Klein, T.; Marcenat, C. Superconducting Group-IV Semiconductors. *Nat. Mater.* **2009**, *8*, 375−382.

(10) Baskaran, G. Resonating Valence Bond Mechanism of Impurity Band Superconductivity in Diamond. *J. Supercond. Novel Magn.* **2008**, *21*, 45−49.

(11) Zhang, G.; Zeleznik, M.; Vanacken, J.; May, P. W.; Moshchalkov, V. V. Metal-Bosonic Insulator-Superconductor Transition in Boron-Doped Granular Diamond. *Phys. Rev. Lett.* **2013**, *110*, 077001.

(12) Bustarret, E.; Kačmarčik, J.; Marcenat, C.; Gheeraert, E.; Cytermann, C.; Marcus, J.; Klein, T. Dependence of the Superconducting Transition Temperature on the Doping Level in Single-Crystalline Diamond Films. *Phys. Rev. Lett.* **2004**, *93*, 237005.

DOI: 10.1021/acsnano.7b01688
ACS Nano 2017, 11, 5358−5366

(13) Bustarret, E. Superconducting Diamond: an Introduction. *Phys. Status Solidi A* **2008**, *205*, 997−1008.
(14) Zhang, G.; Turner, S.; Ekimov, E. A.; Vanacken, J.; Timmermans, M.; Samuely, T.; Sidorov, V. A.; Stishov, S. M.; Lu, Y.; Deloof, B.; Goderis, B.; Van Tendeloo, G.; Van de Vondel, J.; Moshchalkov, V. V. Global and Local Superconductivity in Boron-Doped Granular Diamond. *Adv. Mater.* **2014**, *26*, 2034−2040.
(15) Kenmochi, K.; Sato, K.; Yanase, A.; Katayama-Yoshida, H. Materials Design of Ferromagnetic Diamond. *Jpn. J. Appl. Phys.* **2005**, *44*, L51−L53.
(16) Talapatra, S.; Ganesan, P. G.; Kim, T.; Vajtai, R.; Huang, M.; Shima, M.; Ramanath, G.; Srivastava, D.; Deevi, S. C.; Ajayan, P. M. Irradiation-Induced Magnetism in Carbon Nanostructures. *Phys. Rev. Lett.* **2005**, *95*, 097201.
(17) Remes, Z.; Sun, S.-J.; Varga, M.; Chou, H.; Hsu, H.-S.; Kromka, A.; Horak, P. Ferromagnetism Appears in Nitrogen Implanted Nanocrystalline Diamond Films. *J. Magn. Magn. Mater.* **2015**, *394*, 477−480.
(18) Makarova, T. L. Magnetic Properties of Carbon Structures. *Semiconductors* **2004**, *38*, 615−638.
(19) Wang, Y.; Huang, Y.; Song, Y.; Zhang, X.; Ma, Y.; Liang, J.; Chen, Y. Room-Temperature Ferromagnetism of Graphene. *Nano Lett.* **2009**, *9*, 220−224.
(20) Yan, D.-C.; Chen, S.-Y.; Wu, M.-K.; Chi, C. C.; Chao, J. H.; Green, M. L. H. Ferromagnetism of Double-Walled Carbon Nanotubes. *Appl. Phys. Lett.* **2010**, *96*, 242503.
(21) Ohldag, H.; Esquinazi, P.; Arenholz, E.; Spemann, D.; Rothermel, M.; Setzer, A.; Butz, T. The Role of Hydrogen in Room-Temperature Ferromagnetism at Graphite Surfaces. *New J. Phys.* **2010**, *12*, 123012.
(22) Zhou, J.; Wang, Q.; Sun, Q.; Chen, X. S.; Kawazoe, Y.; Jena, P. Ferromagnetism in Semihydrogenated Graphene Sheet. *Nano Lett.* **2009**, *9*, 3867−3870.
(23) Bernard, M.; Baron, C.; Deneuville, A. About the Origin of the Low Wave Number Structures of the Raman Spectra of Heavily Boron Doped Diamond Films. *Diamond Relat. Mater.* **2004**, *13*, 896−899.
(24) Bourgeois, E.; Bustarret, E.; Achatz, P.; Omnès, F.; Blase, X. Impurity Dimers in Superconducting B-Doped Diamond: Experiment and First-Principles Calculations. *Phys. Rev. B: Condens. Matter Mater. Phys.* **2006**, *74*, 094509.
(25) Sun, Z.; Shi, J.; Tay, B.; Lau, S. UV Raman Characteristics of Nanocrystalline Diamond Films with Different Grain Size. *Diamond Relat. Mater.* **2000**, *9*, 1979−1983.
(26) Lee, S.-T.; Apai, G. Surface Phonons and CH Vibrational Modes of Diamond (100) and (111) Surfaces. *Phys. Rev. B: Condens. Matter Mater. Phys.* **1993**, *48*, 2684−2693.
(27) Ushizawa, K.; Gamo, M. N.; Kikuchi, Y.; Sakaguchi, I.; Sato, Y.; Ando, T. Surface-Enhanced Raman Spectroscopic Study of Hydrogen and Deuterium Chemisorption on Diamond (111) and (100) Surfaces. *Phys. Rev. B: Condens. Matter Mater. Phys.* **1999**, *60*, R5165−R5168.
(28) Bernard, M.; Deneuville, A.; Bustarret, E. Detection of CH_x Bonds from Micro Raman Spectroscopy on Polycrystalline Boron Doped Diamond Electrodes. *Diamond Relat. Mater.* **2002**, *11*, 662−666.
(29) Lafosse, A.; Hoffman, A.; Bertin, M.; Teillet-Billy, D.; Azria, R. Density-of-States Effect on Surface and Lattice Vibrational Modes in Hydrogenated Polycrystalline Diamond. *Phys. Rev. B: Condens. Matter Mater. Phys.* **2006**, *73*, 195308.
(30) Nagaosa, N.; Sinova, J.; Onoda, S.; MacDonald, A. H.; Ong, N. P. Anomalous Hall Effect. *Rev. Mod. Phys.* **2010**, *82*, 1539−1592.
(31) Jakob, G.; Martin, F.; Westerburg, W.; Adrian, H. Evidence of Charge-Carrier Compensation Effects in $La_{0.67}Ca_{0.33}MnO_3$. *Phys. Rev. B: Condens. Matter Mater. Phys.* **1998**, *57*, 10252−10255.
(32) Wagner, P.; Mazilu, D.; Trappeniers, L.; Moshchalkov, V. V.; Bruynseraede, Y. Anomalous Hall Effect in Thin Films of $Pr_{0.5}Sr_{0.5}MnO_3$. *Phys. Rev. B: Condens. Matter Mater. Phys.* **1997**, *55*, R14721−R14724.
(33) Kawarada, H. Hydrogen-Terminated Diamond Surfaces and Interfaces. *Surf. Sci. Rep.* **1996**, *26*, 205−259.
(34) Dubrovinskaia, N.; Wirth, R.; Wosnitza, J.; Papageorgiou, T.; Braun, H. F.; Miyajima, N.; Dubrovinsky, L. An Insight into What Superconducts in Polycrystalline Boron-Doped Diamonds Based on Investigations of Microstructure. *Proc. Natl. Acad. Sci. U. S. A.* **2008**, *105*, 11619−11622.
(35) Zhang, G.; Janssens, S. D.; Vanacken, J.; Timmermans, M.; Vacík, J.; Ataklti, G. W.; Decelle, W.; Gillijns, W.; Goderis, B.; Haenen, K.; Wagner, P.; Moshchalkov, V. V. Role of Grain Size in Superconducting Boron-Doped Nanocrystalline Diamond Thin Films Grown by CVD. *Phys. Rev. B: Condens. Matter Mater. Phys.* **2011**, *84*, 214517.
(36) Graham, M. R.; Adkins, C. J.; Behar, H.; Rosenbaum, R. Experimental Study of the Ioffe-Regel Criterion for Amorphous Indium Oxide Films. *J. Phys.: Condens. Matter* **1998**, *10*, 809−819.
(37) Hamers, R. J.; Tromp, R. M.; Demuth, J. E. Surface Electronic Structure of Si(111)-(7 × 7) Resolved in Real Space. *Phys. Rev. Lett.* **1986**, *56*, 1972−1975.
(38) Assig, M.; Etzkorn, M.; Enders, A.; Stiepany, W.; Ast, C. R.; Kern, K. A 10 mK Scanning Tunneling Microscope Operating in Ultra High Vacuum and High Magnetic Fields. *Rev. Sci. Instrum.* **2013**, *84*, 033903.
(39) Tinkham, M. *Introduction to Superconductivity*; Dover: New York, 2004; pp 75−76.
(40) Dynes, R. C.; Narayanamurti, V.; Garno, J. P. Direct Measurement of Quasiparticle-Lifetime Broadening in a Strong-Coupled Superconductor. *Phys. Rev. Lett.* **1978**, *41*, 1509−1512.
(41) Bulaevskii, L. N.; Buzdin, A. I.; Kulić, M. L.; Panjukov, S. V. Coexistence of Superconductivity and Magnetism: Theoretical Predictions and Experimental Results. *Adv. Phys.* **1985**, *34*, 175−261.
(42) Buzdin, A. I.; Mel'nikov, A. S. Domain Wall Superconductivity in Ferromagnetic Superconductors. *Phys. Rev. B: Condens. Matter Mater. Phys.* **2003**, *67*, 020503.
(43) Anderson, P. W.; Suhl, H. Spin Alignment in the Superconducting State. *Phys. Rev.* **1959**, *116*, 898−900.
(44) Iavarone, M.; Moore, S. A.; Fedor, J.; Ciocys, S. T.; Karapetrov, G.; Pearson, J.; Novosad, V.; Bader, S. D. Visualizing Domain Wall and Reverse Domain Superconductivity. *Nat. Commun.* **2014**, *5*, 4766.
(45) Yang, Z.; Lange, M.; Volodin, A.; Szymczak, R.; Moshchalkov, V. V. Domain-Wall Superconductivity in Superconductor-Ferromagnet Hybrids. *Nat. Mater.* **2004**, *3*, 793−798.
(46) Karapetrov, G.; Belkin, A.; Novosad, V.; Iavarone, M.; Fedor, J.; Pearson, J. E.; Petrean-Troncalli, A. Adjustable Superconducting Anisotropy in Superconductor-Ferromagnet Bilayers. *IEEE Trans. Appl. Supercond.* **2009**, *19*, 3471−3474.
(47) Samuely, T.; Szabó, P.; Komanický, V.; Rodrigo, J. G.; Vieira, S.; Samuely, P. Enhanced Superconductivity in Nanosized Tips of Scanning Tunneling Microscope. *Acta Phys. Pol., A* **2010**, *118*, 1038−1039.

DOI: 10.1021/acsnano.7b01688
ACS Nano 2017, 11, 5358−5366